Towards Optimal Placement of Free-Space Optical Terminal on the Spacecraft Body

Juan A Fraire, Joan A Ruiz-De-Azua, Elena Fernandez-Nino

▶ **To cite this version:**

Juan A Fraire, Joan A Ruiz-De-Azua, Elena Fernandez-Nino. Towards Optimal Placement of Free-Space Optical Terminal on the Spacecraft Body. IEEE Transactions on Aerospace and Electronic Systems, 2024, pp.1-15. 10.1109/TAES.2024.3435176 . hal-04711310

HAL Id: hal-04711310
https://hal.science/hal-04711310v1

Submitted on 26 Sep 2024

HAL is a multi-disciplinary open access archive for the deposit and dissemination of scientific research documents, whether they are published or not. The documents may come from teaching and research institutions in France or abroad, or from public or private research centers.

L'archive ouverte pluridisciplinaire **HAL**, est destinée au dépôt et à la diffusion de documents scientifiques de niveau recherche, publiés ou non, émanant des établissements d'enseignement et de recherche français ou étrangers, des laboratoires publics ou privés.

Towards Optimal Placement of Free-Space Optical Terminal on the Spacecraft Body

Juan A. Fraire*†‡, Joan A. Ruiz-de-Azua§, Elena Fernandez-Nino§
*Inria, INSA Lyon, CITI, UR3720, 69621 Villeurbanne, France
†CONICET - Universidad Nacional de Córdoba, Córdoba, Argentina
‡Saarland University, Saarland Informatics Campus E1 3, 66123 Saarbrücken, Germany
§i2Cat Foundation Space Communications Research Group, Spain

***Abstract*—Free-Space Optical (FSO) links have emerged as a promising solution for enabling high-speed data transfer in networked space systems. These links leverage highly directed optical beams amplified by telescopes that can be oriented using gimbal engines. However, the gimbal's limited swipe range poses a challenge in optimizing the placement of the FSO terminal on the satellite body. This placement directly impacts the feasible contact time, which is constrained by the gimbal motors' degree of freedom and speed as the satellites follow their orbital trajectories. In this paper, we address the problem of optimizing the FSO terminal placement to maximize the aggregate effective contact time with the target. First, we formally describe the problem assumptions and perform baseline case studies to gain valuable insights. Next, we define appropriate metrics that capture the contact time performance to evaluate different placement strategies. Our core contributions are two heuristics, simulated annealing, and an evolutionary genetic algorithm to optimize the FSO terminal placement. We finally demonstrate through extensive simulation and analysis that our proposed optimization approaches can significantly improve the baseline contact time by up to 27.7%. These findings highlight the potential of employing sophisticated optimization techniques to enhance the performance of FSO links.**

***Index Terms*—Free-space optical links, Inter-satellite links, Simulated annealing, Evolutionary genetic algorithm.**

I. Introduction

In the rapidly expanding arena of space communications, high-speed data transfer has become a critical requirement.

Non-Terrestrial Networks (NTN) represent one avenue of this expansion. Real-time global connectivity is imperative to facilitate the anticipated high-speed multimedia services and applications associated with 5G, Beyond-5G (B5G), and 6G technologies [1], [2]. As highlighted in the recent 3GPP Releases and projected cellular and mobile systems, satellites are expected to play a key role as access and core components of NTN [3], [4]. Concurrently, advancements in Earth Observation (EO) constellations are contingent on innovative solutions for data transport [5]. Projected innovations in distributed satellite missions, including novel topologies and agile flight formation techniques, are poised to revolutionize EO [6], [7]. By augmenting observation duration and data acquisition, they present opportunities for developing new applications such as continuous Earth monitoring and disaster management [8], [9]. This transformation requires the transport of large volumes of data back to Earth, potentially leveraging Inter-Satellite Links (ISLs) [9] and intermediate storage systems [10].

Free-Space Optical (FSO) links have surfaced as an influential solution to this demand, providing a capacity that is difficult to match using the limited spectrum available for Radio Frequency (RF) communication [1]. By leveraging highly directed optical beams amplified by telescopes, these Inter-Satellite Links (ISL) and Space-to-Ground Links promise faster data transfer between space and ground systems [11]. However, the practical deployment of FSO technology presents its unique challenges. In this research, our primary focus is the strategic placement of the FSO terminal on a spacecraft. We incorporate the pointing constraints into our decision-making process to increase the accumulated contact time with other spacecraft in the network.

The placement of the FSO terminal significantly impacts the effective contact time for data transmission. Given the limited swipe range of the gimbal engines that orient the FSO terminal, the placement strategy must carefully consider the gimbal motors' degree of freedom as Low-Earth Orbit (LEO) satellites follow their orbital trajectories. This makes the task of FSO terminal placement an intricate optimization problem. It intertwines aspects of orbital propagation, geometric considerations, and technical constraints, which profoundly affect the performance of FSO links in space. Achieving an optimal placement of FSO terminals enhances the efficiency of data transfer in these networks by ensuring maximum contact time and reliable high-speed links, crucial for applications such as remote sensing, disaster management, and real-time global communication. For instance, in the context of 5G and 6G technologies, the enhanced FSO link performance can significantly reduce latency and increase data throughput, enabling seamless integration of terrestrial and non-terrestrial networks.

This paper conducts a comprehensive study focusing on the optimal placement of FSO terminals on spacecraft bodies to maximize contact time within ISL. Unlike existing studies that primarily focus on the general performance of FSO links, our research uniquely addresses the strategic placement of FSO terminals, considering gimbal constraints, to maximize contact time, thereby directly impacting the efficiency of data transfer in networked space systems. Our primary contribution is formulating a unified model framework, effectively integrating aspects of orbital mechanics, spacecraft dynamics, and FSO terminal characteristics. Furthermore, we propose two distinct heuristic strategies based on Simulated Annealing (SA) [12]

and Genetic Algorithms (GA) [13]. These are thoroughly tested through an exhaustive evaluation campaign, which yields compelling evidence of the practical value of pursuing optimal FSO placement solutions.

The subsequent structure of this paper unfolds as follows. Section II provides a comprehensive review of NTN and Earth Observation EO applications and a chronological exploration of research progress in FSO. The specifications and presuppositions for addressing the spacecraft terminal placement are expounded in Section III. The two optimization heuristics, founded on simulated annealing and genetic algorithms, are presented in Section IV. Conclusions and prospective research directions are drawn in Section VI.

II. Background

Research on FSO for space and satellites is plenty and dates back to the late 90s. The pointing, acquisition, and tracking challenges in space FSO was already highlighted by Ho [14] and Baister et al. [15]. The latter authors discussed new applications using FSO between satellites to increase connectivity in a satellite system [16]. They also presented the current status of optical terminals developed for future inter-satellite requirements.

The significance of FSO links has considerably increased since the second decade of the 2000s. Particularly in the context of space-to-ground links, scholars have made noteworthy contributions. Alliss et al. [18] examined atmospheric fade induced by clouds, a crucial factor in FSO links. This work was further expanded by Giggenbach et al. [19], who enhanced the model for satellite-ground communication via FSO links. Pigulevski et al. [20] proposed FSO links as a viable solution to atmospheric effects in space-to-ground communications for both orbital use and deep space exploration. One of the landmark achievements in this field was NASA's Lunar Laser Communication Demonstration (LLCD) in 2013 [21]. The initiative successfully accomplished the first-ever duplex laser communication between a lunar-orbit satellite, LADEE, and Earth-based ground stations.

The sphere of space-to-space FSO links has also garnered considerable interest. For instance, Tang and Wang [22] evaluated service availability for ISL within navigation constellations. Gong et al. [23] explored the concept of ground station diversity to mitigate weather impairments in space-to-ground FSO links. In parallel, Kopp et al. [24] examined the potential of utilizing FSO links in GEO repeater systems to manage large volumes of data collected or generated in remote locations. One significant accomplishment in this domain is the successful deployment of Tesat's FSO transceiver onboard the first European Data Relay System (EDRS-A) GEO satellite [25]. This satellite utilizes space-to-space FSO links to relay data from LEO satellites to the ground.

Most pertinent research in FSO communications was undertaken in the 2020s. Within the space-to-ground FSO links context, Zhang et al. [26] performed a comprehensive review of coherent FSO in light of turbulent atmospheric effects and suggested mitigative strategies against these impairments. Furthermore, the atmospheric attenuation impact on FSO links, encompassing molecular absorption, aerosol scattering, and absorption, was the focus of detailed studies by Giggenbach et al. [27] and Devkota et al. [28]. Atmospheric effects were studied for the space-to-ground FSO links by Yousif, Elsayed et al. in [29]–[32]. Regarding applications, Al-Mohammed et al. [33] proposed an innovative communication approach for ultra-high-speed trains, demonstrating a space-to-ground FSO link with a fixed data rate of 1.25 Gbps or a variable rate. Works in the context of Unmanned Areal Vehicles (UAVs) are also plenty in the literature [34].

In the domain of space-to-space FSO links, Calzolaio et al. [35] highlighted the inauguration of the second node of the EDRS (EDRS-C), which employed FSO links to facilitate real-time relay to LEO satellites at 1.8 Gbit/s in 2020. Tiwari and Chauhan [36] delivered a comprehensive review of FSO communication links in the same year, focusing particularly on inter-satellite links. Chaudhry et al. [37] motivated the potential for low latency in FSO links by presenting results in the context of SpaceX's phase I deployment of Starlink. They further analyzed the influence of temporary FSO ISL links on network latency in emerging satellite networks [38], with extensions to this work later provided in [39]. Rabinovich et al. [40] introduced adaptive waveforms techniques such as N-PSK in FSO links for LEO satellite systems. Follow-up works by the same authors extended the FSO models and discussed their integration within broader network architecture models [41]. In a separate study, Liang et al. [42] provided a thorough link budget analysis for FSO ISL and uplink/downlink. Simultaneously, Goncalves et al. [43] reviewed theoretical research on FSO communications and their integration with Delay and Disruption Tolerant Networking (DTN) in the space context. In 2023, Navitskaya et al. [44] developed a simulation framework for the design, modeling, and analysis of classical and quantum communication systems over terrestrial, ground-satellite, and ISL using FSO links.

Other Related Technologies: FSO links are not the only technology being explored for high-speed data transfer in space networks. Alternative technologies, such as hybrid RF/FSO systems, are also being researched and implemented. Hybrid RF/FSO systems aim to combine the strengths of both RF and FSO technologies, providing reliable communication links with higher data rates [45], [46]. Additionally, emerging technologies like terahertz (THz) communications are being explored for their potential to offer ultra-high-speed data transfer [47], [48]. While the remainder of this paper focuses on FSO, these alternative and complementary technologies highlight the diverse landscape of solutions being investigated to meet the growing demands of space communications.

A. Gap in FSO Terminal Placement

Despite the undeniable surge in interest towards FSO space links across academic, governmental, and industrial sectors, it is noteworthy that all the aforementioned studies presuppose that mission designers autonomously determine the placement of the FSO terminal on the satellite body [49]. In addition, it is essential to highlight that all these studies share a common

Figure 1: FSO terminals in the market as of 2023: a) Mynaric Mk3 terminal, b) MIT Lincoln Laboratory ILLUMA-T terminal, c) Tesat's LCT 135 GEO terminal (used in EDRS), d) Tesat's SmartLCT 70 LEO terminal, and e) Xenesis Xen-Hub terminal [17].

assumption: they do not account for orientation constraints or the use of gimbal-based engines, which are inherently limited in angular speed, to execute a coarse pointing of the telescope.

For example, see some of the currently available FSO terminals for the LEO and GEO segment in Fig. 1 (reported in [17]). It is clear that gimbal motors to rotate the telescope are a fundamental part of the mechanism that needs to be considered. As discussed below, they define the Field of Regard (FoR), which limits the spatial region within which the FSO system can establish communication links [1].

To the best of the authors' understanding, no previous study has investigated and optimized the placement of the FSO terminal on the satellite body while considering the orientation and speed constraints inherent to gimbal mechanisms. However, the terminal's final placement and orientation imply the FoR region's spatial orientation. Therefore, the placement process significantly affects the effective connectivity time.

Indeed, in future FSO systems, the placement of the FSO terminal will not merely be a given but a crucial element of the overall spacecraft's design process, for which no methodology exists yet. This paper covers this gap with simulated annealing and genetic algorithms comprising realistic orbital models and propagators.

III. Models

A. Orbital Elements

Orbital elements are parameters that describe the motion of a satellite in space. They are fundamental descriptors of the satellite's orbit. These elements provide a snapshot of the satellite's position and motion at a specific time (epoch). The position of a satellite at a specific moment in time, known as the *epoch*, is traditionally represented by a set of six parameters. These are known as the Keplerian elements or classical orbital elements.

a) Orbit Size and Shape (a, e): The size and shape of an orbit are specified by the semi-major axis (a) and the eccentricity (e). The semi-major axis is the longest radius in an elliptical orbit or half the distance between the perigee and apogee. The eccentricity, calculated by $e = \sqrt{1 - (b^2/a^2)}$, is a dimensionless parameter that measures the orbit's deviation from a perfect circle, where b is the *semi-minor axis*. In the case of a circular orbit, the semi-major axis a is equal to the orbit's radius. The altitude h of a satellite is defined relative to Earth's surface. Hence, the orbit radius is the sum of the altitude h and Earth's semi-major axis $r_a = 6378.137$ km, as specified in the WGS84 reference system [50].

b) Orbit Orientation (α, Ω, ω): Three angles determine the orientation of the orbital plane in three-dimensional space: the inclination (α), the longitude of the ascending node (Ω), and the argument of perigee (ω). *i*) The *inclination* (α) is the angle between the plane of the orbit and a reference plane, typically the equator. This angle lies within $\alpha \in [0, 2\pi[$. An inclination of $0°$ corresponds to an equatorial orbit where the satellite moves along the equator, whereas a $90°$ inclination represents a polar orbit where the satellite moves over the poles. *ii*) The *longitude of the ascending node* (Ω), or LAN, determines the orientation of the orbit in the horizontal plane. This is the angle from a reference point to the ascending node, where the satellite crosses the equatorial plane from south to north. Depending on the context, this angle is defined differently. When measured in relation to a longitude reference, it is designated as $L_0 \in [-\pi, \pi[$. In this case, Ω can be calculated as $\Omega = L_0 - S_E \cdot t$, where S_E denotes the angular speed of Earth's rotation. Alternatively, when measured from the vernal equinox, it is known as the *right ascension of the ascending node* (RAAN) and ranges within $[-\pi, \pi[$. *iii*) The *argument of Perigee* (ω) defines the orientation of the orbit within its plane. It is the angle from the ascending node to the perigee (the point of closest approach to the central body), measured in the direction of the satellite's motion.

c) Position in Orbit (ν): The position of the satellite in orbit is defined by the true anomaly (ν) is the angle from the perigee to the object's position at any point in its orbit. Alternatively, the mean anomaly (M) is a related angle that increases linearly with time, simplifying the mathematics of orbital motion, particularly for elliptical orbits ($e > 0$). Since the perigee's location is not defined in circular orbits ($e = 0$), an equivalent parameter known as the *argument of latitude* $u \in [-\pi, \pi[$ is often used instead, defining the angle from the ascending node to the spacecraft's current position.

B. Orbital Propagator Model

Orbital propagators are predictive models that use these orbital elements to calculate the future positions and velocities

[1]While this paper primarily focuses on larger FSO terminals, it's important to note that our proposed methods are adaptable to the limited FoR present in nano-satellites, as shown in Figure 1. These smaller platforms typically only use fine-pointing mirrors due to spatial constraints. However, as indicated in our future work considerations, nano-satellites are more amenable to body-pointing techniques than gimbal-based ones.

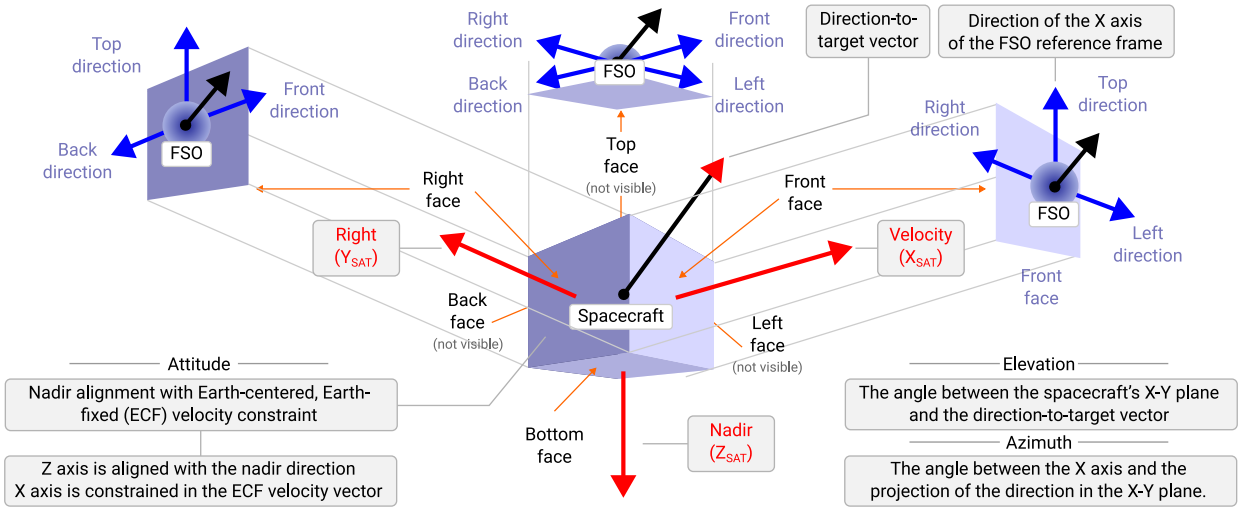

Figure 2: Spacecraft's attitude, reference frame, and baseline placement for FSO terminals. This figure illustrates the default placement of the FSO terminal on the spacecraft, which serves as the baseline solution for comparison with the optimized placements achieved through SA and GA methods studied in Section V.

of satellites over time. Propagators incorporate the effects of various forces acting on the satellite, such as gravitational perturbations, atmospheric drag, and solar radiation pressure, to provide accurate predictions of the satellite's trajectory. Therefore, while the six Keplerian elements describe the spacecraft's position, an orbital propagator is a computational tool that predicts its future or retrospective position and velocity. Our solution was developed to fit the following propagators.

a) Two-Body (2B): One of the simplest and most commonly used orbital propagators is the *two-body propagator* (2B) [51]. In 2B, one body (spacecraft) orbits another (Earth) under the influence of gravitational forces only and where the mass of the orbiting body is negligible compared to the mass of the central body. It analytically solves Kepler's equations, which makes 2B relatively simple and computationally efficient. Still, it neglects the effects of other forces, such as atmospheric drag, solar radiation pressure, or the gravitational pull of other celestial bodies. The 2B Propagator is typically used for satellites with station-keeping capabilities, where orbital perturbations are actively managed through thrusters and attitude control systems. This propagator is suitable for many operational satellites equipped with gimbal-based OISLs, as it provides a computationally efficient model for scenarios where perturbations are minimal.

b) Simplified General Perturbations 4 (SGP4): SGP4 was developed to account for gravitational perturbations, atmospheric drag, and solar radiation pressure effects on the motion of satellites in near-Earth space [52]. It utilizes a set of Keplerian elements, Two-Line Elements (TLEs), provided by the North American Aerospace Defense Command (NORAD). As a semi-analytical algorithm, SGP4 achieves a trade-off between accuracy and computational efficiency and is particularly suited for LEO satellites [53]. However, it is less accurate for propagation over extended time-frames due to its inability to account for certain perturbations, such as tides from the Sun and Moon [54]. The SGP4 model is widely used for tracking LEO satellites, particularly those without frequent station-keeping maneuvers. SGP4 is a balanced choice for accuracy and computational efficiency in short to medium-term predictions.

c) High-Precision Numerical Propagators: The Runge-Kutta 4th order (RK4) [55] propagator numerically solves the equations of motion without making any simplifying assumptions. It is capable of handling complex and high-accuracy requirements. However, this increased accuracy comes at the cost of higher computational intensity. Another powerful numerical propagator is the Gauss-Legendre method, known for its superior performance in long-term integrations [56]. These methods are employed for missions that require precise long-term predictions. For example, these propagators are essential for interplanetary missions or geostationary satellites experiencing complex perturbations from multiple gravitational sources. While computationally intensive, these high-precision models ensure accurate trajectory predictions necessary for critical mission phases and long-duration space operations.

C. Spacecraft Attitude Model

The platform model involves the orientation of the LEO satellite body frame with respect to the Earth-centered frame (a.k.a. attitude). The model is illustrated in Fig. 2. This work assumes the spacecraft's attitude is aligned with the nadir vector, pointing toward the Earth's center, within an Earth-Centered, Earth-Fixed (ECEF) coordinate system under a velocity constraint. This postulation entails the spacecraft's X_{SAT}-axis corresponding with the velocity vector, typically directed along the trajectory. The Z_{SAT}-axis coincides with the vector extending from the spacecraft towards the Earth's center. Lastly, the Y-axis is established by the cross-product of the unitary direction vectors along the X_{SAT} and Z_{SAT} axes. This is the most common attitude used in nominal LEO satellite operations.

The presumption throughout this analysis is that this specific attitude remains constant throughout the LEO satellite's trajec-

tory. This assumption is grounded in the operational reality of most LEO satellites, where EO instruments and ground antennas are typically equipped on the Z_{SAT} face, maintaining constant alignment toward Earth's center. Active Attitude and Orbit Control Systems (AOCS) preserve this orientation [51]. These systems employ sensors (like sun sensors, star trackers, or gyroscopes) to measure the spacecraft's current state and actuators (like thrusters or reaction wheels) to guarantee the satellite platform's stability and orientation.

D. FSO Terminal Model

Minimal and maximal angular extents of elevation and azimuth characterize the FSO gimbal model. These angular parameters are measured in the FSO reference frame and delineate the FoR of the FSO terminal, thus establishing its potential spatial communication range.

a) FSO Terminal Reference Frame: The configuration of the FSO terminal's reference frame is such that the X_{FSO} axis aligns with the telescope's forward direction at rest. The Z_{FSO} axis corresponds to the terminal's uppermost point, lying perpendicular to the spacecraft's side. The final component of the Y_{FSO} axis is derived from the cross-product of the previous two axes. This layout constitutes the standard orientation for the FSO terminal in its stand-by state, providing a frame of reference for all subsequent movements and adjustments. Fig. 3 offers a visual depiction of this reference frame, providing a clear understanding of the terminal's physical orientation within the spacecraft

b) Field of Regard: The FoR in FSO terminals defines the comprehensive region in space within which the system can establish potential communication links (i.e., link budget achieved). The extent of this area is dictated by the mechanical, electronic, and communication capabilities of the system to physically steer or reorient its telescope or laser beam in both the azimuth (ψ_{gmb}) and elevation (θ_{gmb}) planes. The boundaries of this FoR are set by the minimum and maximum achievable azimuth and elevation angles, specifically $\theta_{gmb}^{\min}$, $\theta_{gmb}^{\max}$, $\psi_{gmb}^{\min}$, and $\psi_{gmb}^{\max}$. These limits determine the spatial extent over which the terminal can retain a line-of-sight connection with other communication terminals, thus defining the operational capabilities of the FSO system. Fig. 3 visually represents the azimuth and elevation angles within the FSO gimbal's reference frame, illustrating these essential operational parameters.

c) Gimbal Speed: Moreover, the gimbal engines inherently limit the rates at which azimuth and elevation can change, denoted as $\dot{\psi}_{gmb}^{\max}$ and $\dot{\theta}_{gmb}^{\max}$, respectively. These limitations are particularly critical in dynamic environments such as space, where the terminal and its communicating entities might experience rapid and unpredictable relative movements. Furthermore, these constraints can have implications for the system's energy consumption. Since the gimbal engines must work harder to maintain pointing accuracy in fast relative motion, more power may be required. This creates a complex optimization problem, with the system aiming to simultaneously minimize energy use while maximizing performance and maintaining system stability.

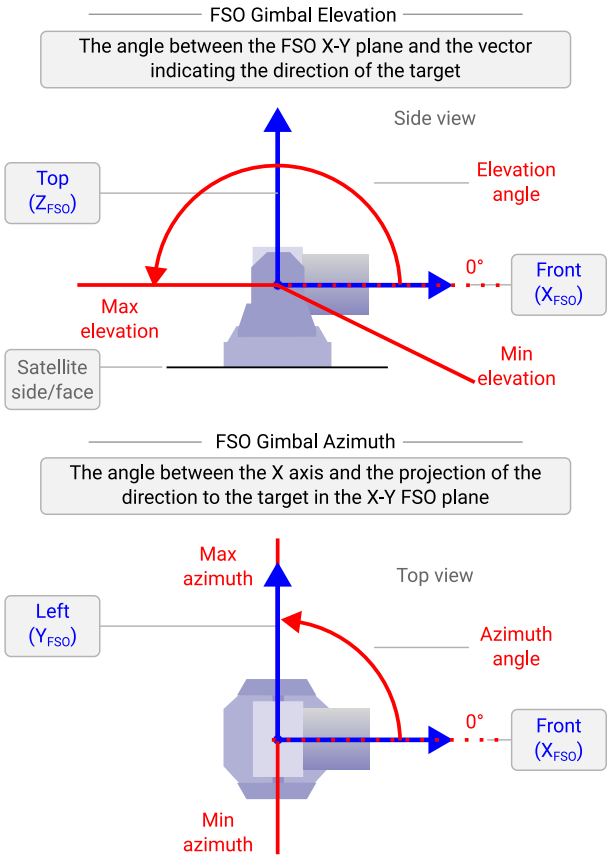

Figure 3: FSO terminals FoR determined by gimbal's elevation (θ_{gmb}) and azimuth (ψ_{gmb}) angles constrained by $\theta_{gmb}^{\min}$, $\theta_{gmb}^{\max}$, and $\psi_{gmb}^{\min}$, $\psi_{gmb}^{\max}$, respectively.

d) Gimbal Lock: A critical design aspect of gimbal systems is overlapping azimuth and elevation ranges within the FoR space. When both azimuth and elevation engines have overlapping operational ranges, it introduces the potential for ambiguous pointing solutions; the same point in the FoR can be reached through different $(\theta_{gmb}, \phi_{gmb})$ angle pairs. This condition, known as *gimbal lock* or *gimbal singularity*, can pose significant challenges to the system control scheme [57]. It can lead to unexpected and rapid movements when the system switches between these multiple solutions to orient towards the same point in space. If the pointing strategy is not adequate, this could result in performance degradation or even mechanical stress and damage to the gimbal mechanism.

e) Optical Channel Acquisition: The process of optical channel acquisition deals with establishing a communication link between two FSO terminals. This process involves steps as discussed in relevant literature [14], [36], [58]. *i*) Coarse pointing: the terminal approximates the direction of the target terminal based on initial estimates using the gimbal motors. *ii*) Fine pointing: the terminal transitions into a fine-pointing phase, wherein it precisely adjusts its pointing direction until the target terminal is accurately located within its field of view. There are generally two modes of operation for the fine-pointing phase: *beacon* mode (target terminal emits a divergent beacon signal) and *beaconless* mode (target ter-

minal spirals along the uncertainty region). Using a beacon can expedite the acquisition process and introduce additional system complexity. *iii*) Synchronization: the terminals attempt to synchronize their communication protocols, including clock rates, frame structure, etc. Overall, the process of optical channel acquisition is a complex and critical aspect of FSO communications. We consider the practical measurements reported for the EDRS system in [58] to model the overall acquisition sequence time τ_{acq}. Inspired by the EDRS system parameters, we choose $\tau_{acq} = 100$ seconds to account for safe margins in other less mature systems. As detailed in the following sections, the effective contact time will be calculated by deducting the acquisition time, denoted as τ_{acq}, for every initiation of a contact session. Note that this study focuses on optimizing of FSO terminal placement for ISL in space-to-space communication scenarios. Therefore, physical layer characteristics such as turbulence-induced fading and path loss due to atmospheric conditions are not considered, as these factors are not relevant in the vacuum of space where ISL operates.

E. Terminal Placement Model

In the context of FSO terminal placement, it is significant to note that the terminal's reference frame (X_{FSO}, Y_{FSO}, Z_{FSO}) is rotated with respect to the satellite platform reference frame (X_{SAT}, Y_{SAT}, Z_{SAT}), both discussed above. Bear in mind that the FSO rotation with respect to the satellite body's frame is the core object of study in this paper, as it will directly define the orientation of the FSO's FoR space and, thus, the overall feasible contact time from the FSO terminal. In this paper, we distinguish two approaches to express this rotation.

a) Euler Angles ($\psi_{FSO}, \theta_{FSO}, \phi_{FSO}$): This relative positioning between the terminal and the satellite platform is governed by azimuth (ψ_{FSO}), elevation (θ_{FSO}), and roll (ϕ_{FSO}) angles. The azimuth, or ψ_{FSO}, denotes the rotation around the Z_{FSO} axis, while the elevation, or θ_{FSO}, signifies the rotation around the Y_{FSO} axis. Finally, the roll, represented by ϕ_{FSO}, delineates the rotation around the X_{FSO} axis. In this way, the tuple $(\psi_{FSO}, \theta_{FSO}, \phi_{FSO})$ can be used to define the FSO terminal placement in the spacecraft body.

b) Quaternions ($\mathbf{q} = q_{wFSO} + q_{xFSO}\mathbf{i} + q_{yFSO}\mathbf{j} + q_{zFSO}\mathbf{k}$): Even though the wide and intuitive usage of azimuth, elevation, and roll angles for this type of orientation representation, another potent approach is employing quaternions. Quaternions are represented as $\mathbf{q} = q_{wFSO} + q_{xFSO}\mathbf{i} + q_{yFSO}\mathbf{j} + q_{zFSO}\mathbf{k}$, where q_{wFSO} is referred to as the scalar part or real part (it encodes the amount of rotation around the axis specified by the vector part), and q_{xFSO}, q_{yFSO}, q_{zFSO} are referred to as the vector part or imaginary part (they form a 3D vector that points along the axis of rotation). Quaternions extend the concept of rotation in three dimensions and offer an effective way to encapsulate the information of rotational transformations. They are especially advantageous in mitigating problems such as gimbal locks associated with Euler angles. Gimbal lock is a phenomenon that occurs when the axes of a three-dimensional gimbal system align, causing a loss of one degree of freedom and thus making a certain orientation unachievable. Quaternions, in contrast, provide a four-dimensional representation that avoids this issue and facilitates operations. While we use quaternions in our terminal placement model, we prefer Euler angles as input and output to facilitate the intuition illustrated in Fig. 3.

c) Baseline Terminal Placement: This study represents the first attempt to employ heuristic optimization techniques for the placement of LCTs on spacecraft bodies. As there are no directly comparable studies, we used the default placements on the spacecraft's flat faces as our baseline. We identified sixteen prevalent placement options that include three distinct configurations on each of the spacecraft's four faces (front, back, left, and right) as well as four placements on the top face of the spacecraft, assumed to maintain a nadir-aligned attitude with ECEF velocity constraint. These baseline placements are graphically depicted in Fig.2. In the forthcoming Section IV, we shall employ heuristics to probe the entire three-dimensional solution space, denoted as $(\psi_{FSO}, \theta_{FSO}, \phi_{FSO})$, aiming to improve the contact time efficacy of the FSO terminal.

F. Target Vector Model

Satellite propagators discussed in Section III B provide the azimuth and elevation vectors towards the target node (spacecraft or ground station) as seen from the source spacecraft's reference frame $(\psi_{tgt}^{SC}, \theta_{tgt}^{SC})$. To assess the pointing capability of the FSO terminal gimbal towards the target, it is crucial to transpose these angles into the FSO terminal's reference frame $(\psi_{tgt}^{FSO}, \theta_{tgt}^{FSO})$. These can then be compared with $\theta_{gmb}^{\min}$, $\theta_{gmb}^{\max}$, $\psi_{gmb}^{\min}$, and $\psi_{gmb}^{\max}$ to determine FSO link feasibility.

a) Reference Frame Transformation: The conversion procedure commences with defining the FSO placement's coordinates, X_{FSO}, Y_{FSO}, and Z_{FSO}, as unit vectors anchored in the spacecraft's reference frame. The transformation matrix bridging the FSO frame to the spacecraft frame, denoted by $T_{FSO\to SC}$, is then expressed as follows:

$$T_{FSO\to SC} = \begin{bmatrix} X_{FSO}[0] & Y_{FSO}[0] & Z_{FSO}[0] \\ X_{FSO}[1] & Y_{FSO}[1] & Z_{FSO}[1] \\ X_{FSO}[2] & Y_{FSO}[2] & Z_{FSO}[2] \end{bmatrix}. \quad (1)$$

The inverse of this matrix yields the transformation from the spacecraft to the FSO frame, symbolized as $T_{SC\to FSO} = (T_{FSO\to SC})^{-1}$.

b) Target Vector Transformation: Subsequently, the target's direction from the spacecraft's perspective, denoted D_{tgt}^{SC}, can be represented using azimuth and elevation angles as follows:

$$D_{tgt}^{SC} = \begin{bmatrix} \cos(\psi_{tgt}^{SC}) \cdot \cos(\theta_{tgt}^{SC}) \\ \sin(\psi_{tgt}^{SC}) \cdot \cos(\theta_{tgt}^{SC}) \\ \sin(\theta_{tgt}^{SC}) \end{bmatrix} = \mathbf{T} \cdot A, \quad (2)$$

where matrix $A = \begin{bmatrix} \psi_{tgt}^{SC} & \psi_{tgt}^{SC} & \theta_{tgt}^{SC} \end{bmatrix}$, and $\mathbf{T} = \begin{bmatrix} \cos(\cdot) \cdot \cos(\cdot) & \sin(\cdot) \cdot \cos(\cdot) & \sin(\cdot) \end{bmatrix}$.

Hence, D_{tgt}^{SC} can be transformed into the FSO reference frame using the equation $D_{tgt}^{FSO} = T_{SC\to FSO} \cdot D_{tgt}^{SC}$. Finally,

the azimuth and elevation to the target measured in the FSO frame can be computed as

$$\psi_{tgt}^{FSO} = \text{atan2}(D_{tgt}^{FSO}[1], D_{tgt}^{FSO}[0]),$$
$$\theta_{tgt}^{FSO} = \text{atan2}\left(D_{tgt}^{FSO}[2], \sqrt{D_{tgt}^{FSO}[0]^2 + D_{tgt}^{FSO}[1]^2}\right). \quad (3)$$

G. Contact Time Model

The essential objective of the FSO placement optimization problem lies in maximizing the link contact time. We define *contact time* τ as the cumulative duration during which the FSO terminal's gimbals can sustain their aim at the target spacecraft or terrestrial node within a specified topological timeframe defined by $\mathcal{T}$. Nevertheless, to accurately emulate the communication phenomena, the contact time must be adjusted to account for the overhead associated with link acquisition.

Algorithm 1: Effective Contact Time Calculation, `Et()`

Data: FSO placement $\mathcal{F} = (\theta_{FSO}^{curr}, \psi_{FSO}^{curr}, \phi_{FSO}^{curr})$,
Sequence of target vector $\mathcal{S} = (\{\psi_{tgt}^{SC}\}, \{\theta_{tgt}^{SC}\})$
Result: Effective Contact Time τ_{eff}

1 $\tau_{\text{eff}} \leftarrow 0$ `// Effective contact time`
2 **for** t *in* $\{\mathcal{T}\}$ **do**
`/* Compute direction in FSO frame */`
3 $\psi_{tgt}^{FSO}, \theta_{tgt}^{FSO} \leftarrow$ `Cd(`$\mathcal{F}$, ψ_{tgt}^{SC}, ψ_{tgt}^{SC}`)` `// eq.(1-3)`
`/* Attempt alternative if gimbal lock */`
4 **if** $\psi_{tgt}^{FSO}, \theta_{tgt}^{FSO} \notin (\psi_{gmb}^{\min}, \psi_{gmb}^{\max}), (\theta_{gmb}^{\min}, \theta_{gmb}^{\max})$ **then**
5 **if** $-\theta_{tgt}^{FSO} - 2\pi \notin (\theta_{gmb}^{\min}, \theta_{gmb}^{\max})$ **then**
6 $\psi_{tgt}^{FSO}, \theta_{tgt}^{FSO} \leftarrow \psi_{tgt}^{FSO} - 2\pi, -\theta_{tgt}^{FSO} - 2\pi$
`/* Check feasibility and accumulate */`
7 **if** $\psi_{tgt}^{FSO}, \theta_{tgt}^{FSO} \in (\psi_{gmb}^{\min}, \psi_{gmb}^{\max}), (\theta_{gmb}^{\min}, \theta_{gmb}^{\max})$ **then**
8 **if** $\dot{\theta}_{gmb}, \dot{\psi}_{gmb} < \dot{\theta}_{gmb}^{\max}, \dot{\psi}_{gmb}^{\max}$ **then**
9 $\tau_{\text{eff}} \leftarrow \tau_{\text{eff}} + t_s$
`/* Affect link acquisition overhead */`
10 **if** $t - t_{t-1} > t_s$ **then**
11 $\tau_{\text{eff}} \leftarrow \tau_{\text{eff}} - \tau_{acq}$ `// New contact started`

a) Effective Contact Time (τ_{eff}): The effective contact time, represented as τ_{eff}, is the duration of contact time, adjusted to account for the overhead imposed by the optical channel acquisition, denoted as τ_{acq}. Although τ_{eff} is expressed in time units, we also present it as a percentage of the total duration to facilitate comparisons across different periods. Algorithm 1 presents the procedure for computing τ_{eff}. Given the frequent use of this metric in the methods discussed in Section IV, we shall designate this calculation as `Et`($\mathcal{F}$, $\mathcal{S}$) for brevity and clarity. The procedure receives as input the current FSO placement, denoted as ($\mathcal{F} = \theta_{FSO}^{curr}, \psi_{FSO}^{curr}, \phi_{FSO}^{curr}$), and the evolving target vector, represented as ($\mathcal{S} = (\{\psi_{tgt}^{SC}\}, \{\theta_{tgt}^{SC}\})$). The angle evolution represents a discrete-time sample of the angles with a time step denoted by t_s. The required angles can be computed using any of the propagator models discussed in Section III-B. Indeed, the adaptability to various propagator models represents a significant strength of our model.

The algorithm initializes τ_{eff} and performs iterations over all samples in $\mathcal{S}$ up until the topology horizon in $\{\mathcal{T}\}$ is reached (lines 1-2). The first step of each iteration involves computing the target vector's direction in the FSO terminal's reference frame. This computation is facilitated by the `Cd()` function, which effectively executes Equations (1)-(3) (line 3). Next, if the target's azimuth and elevation angles in the FSO terminal reference frame ($\psi_{tgt}^{FSO}, \theta_{tgt}^{FSO}$) fall outside the gimbal range, we utilize the concept of gimbal duality, as discussed in Section III-D *d)* (line 4). Specifically, we try to find alternative azimuth (ψ) and elevation (θ) values that point to the same direction but represent a different tuple of gimbal angles (lines 5-6). Subsequently, the algorithm evaluates the feasibility of the gimbal motors positioning to $\psi_{tgt}^{FSO}, \theta_{tgt}^{FSO}$ (line 7). Additionally, the algorithm checks if the rate of change for the azimuth and elevation motors ($\dot{\theta}_{gmb}, \dot{\psi}_{gmb}$) adheres to the maximum limit constraints (line 8). If these conditions are satisfied, a feasible link is established for the current time step of duration t_s, which is then accumulated in τ_{eff} (line 9). Finally, the `Et()` procedure assesses whether the time gap since the previous time step exceeds t_s (line 10). If it does, this implies the commencement of a new contact. Consequently, an overhead penalty is applied to account for this transition (line 11).

To offer preliminary insight into the irregular τ_{eff} solution space, we refer to Fig. 4, which graphically depicts τ_{eff} fluctuations in the LEO-GEO scenario discussed further in Section V. This representation underscores the intricacy of identifying the optimal FSO terminal placement, necessitating considering many parameters and variables, thus reinforcing the need for robust heuristic strategies that employ advanced algorithmic approaches. A comprehensive list of significant parameters and variables pertinent to the FSO placement model is available in Table I.

IV. Heuristics

Heuristics are problem-solving approaches that provide practical and efficient solutions when analytical solutions are computationally infeasible or may not exist (e.g., they involve numerical processes from orbital propagators or present discontinuities as in the gimbal angle range). In this case, we leverage a Simulated Annealing (SA) heuristic [12]. SA is a probabilistic optimization method inspired by annealing in metallurgy, which involves controlled cooling. Also, we compare with a Genetic Algorithm (GA) approach [13]. GA is a heuristic search technique that mimics the process of natural selection and genetics, using operations like mutation, crossover (recombination), and selection to evolve a population of candidate solutions.

Rationale for Selecting SA and GA: SA and GA were chosen for this study because they are suitable for solving complex optimization problems with non-linear, multi-dimensional search spaces, such as the FSO terminal placement problem. SA's adaptability allows it to escape local optima by probabilistically accepting worse solutions, making

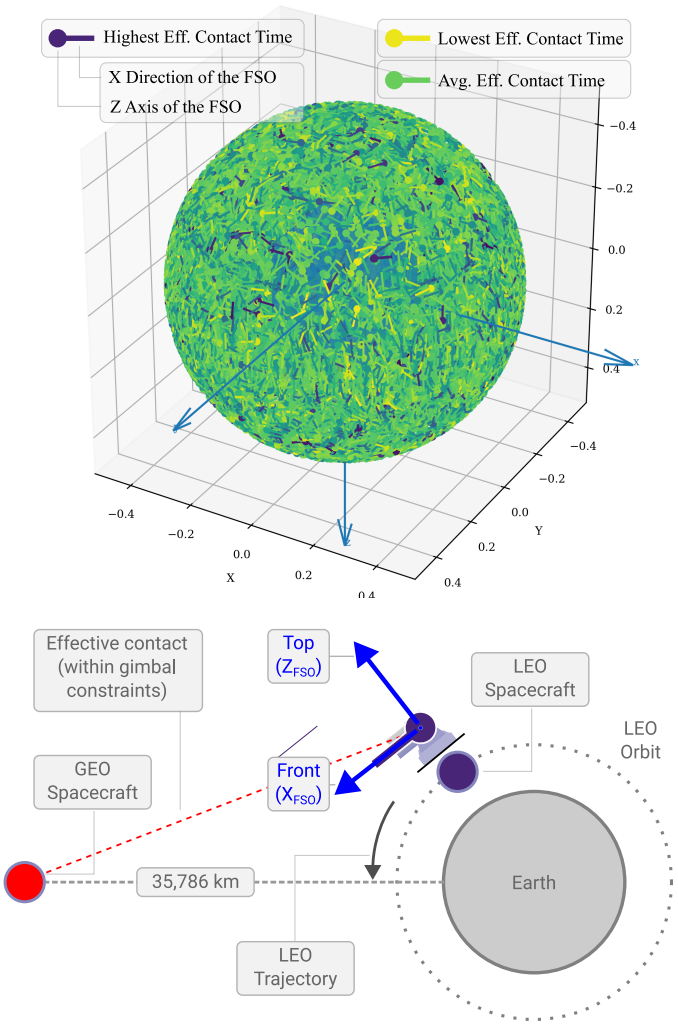

Figure 4: FSO placement solution space. On the top, the units for the X, Y, and Z axes are normalized coordinates, representing the possible Z_{FSO} orientations for placing the FSO terminal on the spacecraft body. The marker "–" indicates the X_{FSO} orientation of the FSO terminal, with the X direction representing the horizontal alignment and the Z axis representing the vertical alignment. The colors represent the effective contact time, with purple indicating the highest effective contact time, yellow indicating the lowest, and green indicating the average. This figure applies to the LEO-GEO communication scenario depicted at the bottom.

it effective for the non-convex nature of the FSO terminal placement problem. Its simplicity and minimal parameter tuning make it robust across various problem instances. GA's population-based approach explores a wide solution space simultaneously, reducing the likelihood of being trapped in local optima. The flexibility to modify genetic operators and the natural parallelism of GA make it scalable and efficient for this application. Both algorithms were adapted to incorporate the effective contact time as the objective function, considering the constraints of gimbal range and speed.

Parameters for SA and GA were tuned to balance exploration and exploitation, and feasibility checks ensured the

Table I: List of Parameters and Variables

Parameter	Description	Units
Orbital Parameters		
a	Semi-Major Axis ($a = 6378.137 + h$)	km
e	Eccentricity	-
α	Inclination	deg
Ω	Longitude of the Ascending Node (LAN)	deg
ω	Argument of Perigee (AOP)	deg
ν	True Anomaly	deg
$\mathcal{P}$	Propagator $\in$ {2B, SGP4, RK4}	-
FSO Terminal Parameters		
$\theta_{gmb}^{\min}, \theta_{gmb}^{\max}$	Min/Max Gimbal Elevation	deg
$\psi_{gmb}^{\min}, \psi_{gmb}^{\max}$	Min/Max Gimbal Azimuth	deg
$\dot{\theta}_{gmb}^{\max}$	Maximum Gimbal Elevation Speed	deg/s
$\dot{\psi}_{gmb}^{\max}$	Minimum Gimbal Azimuth Speed	deg/s
τ_{acq}	Optical Channel Acquisition	s
FSO Terminal Placement Variables		
θ_{FSO}	FSO Terminal Elevation wrt. Spacecraft	deg
ψ_{FSO}	FSO Terminal Azimuth wrt. Spacecraft	deg
ϕ_{FSO}	FSO Terminal Roll wrt. Spacecraft	deg
q_{wFSO}	Scalar part of the quaternion	-
q_{xFSO}	X-component of quaternion's vector part	-
q_{yFSO}	Y-component of quaternion's vector part	-
q_{zFSO}	Z-component of quaternion's vector part	-
FSO/SC Reference Frame Conversion Variables		
$\psi_{tgt}^{SC}, \theta_{tgt}^{SC}$	Az/El to target from spacecraft	deg
$\psi_{tgt}^{FSO}, \theta_{tgt}^{FSO}$	Az/El to target from FSO terminal	deg
$T_{SC \to FSO}$	Spacecraft to FSO transform matrices	-
D_{tgt}^{SC}, D_{tgt}^{FSO}	Target vector direction	-
Time Variables and Metrics		
$\mathcal{T}$, t_s	Topology time horizon and time step	s
τ_{eff}	Effective contact time	s

Table II: Parameters for SA and GA

Algorithm	Parameter	Value
Simulated Annealing	Number of iterations ($\mathcal{I}_{\max}$)	100
	Initial temperature ($\epsilon^{\max}$)	100
	Cooling rate (cr)	0.03
Genetic Algorithm	Number of generations ($\mathcal{G}$)	7
	Population size ($\mathcal{P}_s$)	16
	Tournament size (S)	2
	Mutation rate (Δ_r)	0.5
	Mutation range (Δ_d)	10°
	Elite population count (e)	1

solutions' practical implementability. Parameters we found worked better for both methods in space-to-space scenarios are listed in Table II and described below. Our SA solution is listed in Algorithm 2, while GA is in Algorithm 3. As discussed in the remainder of this section, SA and GA offer robust methods for tackling the FSO placement problem by exploring the solution space to find near-optimal solutions.

A. Simulated Annealing

a) Initial solution: The SA procedure commences with the acquisition of an initial solution for the FSO placement parameters, namely, elevation (θ), azimuth (ψ), and roll (ϕ). This is achieved through the utilization of a uniform random function (U()), subject to the constraints imposed by the ranges of elevation, azimuth, and roll (as depicted in lines 1-3). We

have also explored initial solutions derived from alternative strategies, such as the optimal baseline placement (refer to Section III-E-c)). However, this did not yield any significant differential impact on the performance. Next, the effective contact time τ_{eff} is computed for this placement using the Et() function discussed above (line 4).

Algorithm 2: SA for FSO Placement

Data: Number of iterations $\mathcal{I}_{\max}$, Initial temperature $\epsilon^{\max}$, Cooling rate cr

Result: FSO terminal placement (θ_{FSO}, ψ_{FSO}, ϕ_{FSO})

```
/* Compute initial solution */
1  θ_FSO ← θ_FSO^curr ← U(0, 2π)          // Initial elevation
2  ψ_FSO ← ψ_FSO^curr ← U(−π/2, π/2)      // Initial azimuth
3  φ_FSO ← φ_FSO^curr ← U(−π, π)          // Initial roll
/* Compute effective contact time */
4  τ_eff ← Et(θ_FSO^curr, ψ_FSO^curr, φ_FSO^curr)
/* Iterate */
5  for i in I_max do
       /* Compute temperature */
6      ϵ ← ϵ^max · exp(−cr · i)
       /* Compute new neighbor */
7      λ ← ϵ/ϵ^max                      // Angle span scaling factor
8      θ_FSO^nbr ← U(θ_FSO^curr − π/λ, θ_FSO^curr + π/λ)
9      ψ_FSO^nbr ← U(ψ_FSO^curr − π/(2λ), ψ_FSO^curr + π/(2λ))
10     φ_FSO^nbr ← U(φ_FSO^curr − π/λ, φ_FSO^curr + π/λ)
       /* Compute neighbor eff. contact time */
11     τ_eff^nbr ← Et(θ_FSO^nbr, ψ_FSO^nbr, φ_FSO^nbr)
       /* If the neighbor has better metric */
12     if τ_eff^nbr > τ_eff then
           /* Update best with neighbor */
13         θ_FSO ← θ_FSO^curr ← θ_FSO^nbr      // New elevation
14         ψ_FSO ← ψ_FSO^curr ← ψ_FSO^nbr      // New azimuth
15         φ_FSO ← φ_FSO^curr ← φ_FSO^nbr      // New roll
16     else
           /* Accept neighbor with probability */
17         π ← exp((τ_eff^nbr − τ_eff)/ϵ)
18         if ρ < π then
19             θ_FSO^curr, ψ_FSO^curr, φ_FSO^curr ← θ_FSO^nbr, ψ_FSO^nbr, φ_FSO^nbr
```

b) Iterations: The SA algorithm is designed to run for a fixed number of iterations, denoted as $\mathcal{I}_{\max}$ (line 5). At the outset of each iteration, the algorithm computes the system temperature. The computation utilizes the initial temperature parameter, $\epsilon^{\max}$, and the cooling rate, cr. The temperature experiences an exponential decrease in correspondence with the advancing iterations (line 6).

c) New Neighbor: Subsequently, the algorithm calculates a new 'neighbor' solution in the next phase (lines 7-10). The computation of θ_{FSO}^{nbr}, ψ_{FSO}^{nbr}, and ϕ_{FSO}^{nbr} is conducted in such a manner that a factor, λ control the span of angle variation. Specifically, λ bears a direct proportionality to the decreasing temperature. This strategy has proven advantageous in the FSO placement problem, as it permits fine-grained movements toward the end of the iterations. The allowance for such precision facilitates thorough solution space exploration, characterized by rapidly fluctuating values. The resultant λ effectively modulates the range of angles for the new neighbor solution. At this point, it is worth noting that we can introduce additional neighbor filtering to exclude potential regions for FSO placement, particularly on spacecraft surfaces, such as solar panels, where deployment is not possible. Once more, the τ_{eff}^{nbr} is computed for the new neighbor (line 11).

d) Update or Possibly Accept: If the newly computed 'neighbor' solution demonstrates a superior effective contact time (τ_{eff}) relative to the optimum, it is designated as the new current neighbor (line 12)). Concurrently, the optimal placement parameters, θ_{FSO}, ψ_{FSO}, and ϕ_{FSO} are updated to reflect this superior solution (lines 13-16). Should the new 'neighbor' solution not surpass the current optimal effective contact time (τ_{eff}), it may still be accepted as the prevailing 'neighbor' albeit with a probability that is proportional to its metric (τ_{eff}^{nbr}) and inversely proportional to the temperature (ϵ) (line 17). Upon confirmation of these probabilities, the current 'neighbor' set of angles – θ_{FSO}^{curr}, ψ_{FSO}^{curr}, and ϕ_{FSO}^{curr} – is updated, replacing the previous values with the newly derived ones.

e) Termination: The algorithm terminates with the best found FSO terminal placement in (θ_{FSO}, ψ_{FSO}, ϕ_{FSO}).

B. Genetic Algorithm

a) Initial Population: The GA commences its operations by generating a collection of candidates, or population denoted as $\{\mathcal{P}\}$, containing $\mathcal{P}_s$ entities (lines 1-6). Like the SA process, these entities are generated using a uniform random function, U(). Each newly generated individual is subsequently appended ($\oplus$) to the population. Baseline positions can also be utilized during this process, although no significant benefit was proven during the evaluation. For this case, the population size $\mathcal{P}_s$ should be set to 16 to accommodate the baseline placements illustrated in Fig 2. The baseline solution represents the default placement of the FSO terminal on the spacecraft, chosen based on practical considerations and industry standards. This default placement serves as a reference point for assessing the benefits of the SA/GA-assisted optimization. By comparing the optimized placements with the baseline, we demonstrate the improvements in effective contact time and overall performance.

b) Iterations: The GA algorithm then proceeds to iterate through $\mathcal{G}$ generations (line 7). During each iteration, the fitness of every individual, represented by τ_{eff}, is computed by invoking Et() on the three angles characterizing each candidate p (lines 8-9).

c) Crossover: Subsequently, an appropriate set of parents from Λ is selected to execute the crossover operation (lines 10-13). Firstly, a tournament selection is conducted using a random sampling function, Rs(S, $\mathcal{P}$), which uniformly selects S distinct individuals from $\mathcal{P}$ at random (line 12). The individuals exhibiting superior performance are then conserved in Λ (line 13). Following this, offspring are calculated and stored in $\mathcal{O}$ (lines 14-19). Here, parent pairs (p_1, p_2) are sequentially extracted from Λ (line 15). A crossover point

cp is identified (line 16) through the random integer function Ri(1,3), determining which of the $p.\theta_{FSO}, p.\psi_{FSO}, p.\phi_{FSO}$ angles will be inherited from p_1 or p_2. The resultant two offspring are subsequently appended to $\mathcal{O}$ (lines 17-18). Lastly, an elitist strategy [59] is employed to ensure the preservation of the most optimal individuals. To this effect, $\{\mathcal{P}\}$ is organized in decreasing order of τ_{eff} (sorted()), and the leading e individuals are retained. In contrast, the remaining individuals are replaced by the offspring from $\mathcal{O}$ (line 19).

d) Mutation: The concluding stage in the GA sequence entails mutation (lines 20-24). Every angle from $p.\theta_{FSO}, p.\psi_{FSO}, p.\phi_{FSO}$ within each individual p is subjected to a mutation probability dictated by the mutation rate parameter Δ_r (lines 20-22). If the probability is satisfied, the corresponding angle undergoes a perturbation using a uniform distribution $\mathrm{U}(-\Delta_d, \Delta_d)$, bound by the mutation range Δ_d. As with the neighbor computation in the SA solution, this point of the GA solution also allows for specific filtering. This can prevent the selection of FSO placements that are incompatible with the spacecraft architecture.

Algorithm 3: GA for FSO Placement

Data: Number of generations $\mathcal{G}$, Population size $\mathcal{P}_s$, Tournament size S, Mutation rate Δ_r, Mutation range Δ_d, Elite population count e
Result: FSO terminal placement (θ_{FSO}, ψ_{FSO}, ϕ_{FSO})

/* Initialize population */
1 $\{\mathcal{P}\} \leftarrow \{\}$
2 **for** $p = 0$ *to* $\mathcal{P}_s$ **do**
3 $\quad p.\theta_{FSO} \leftarrow \theta_{FSO}^{curr} \leftarrow \mathrm{U}(0, 2\pi)$ // Elevation
4 $\quad p.\psi_{FSO} \leftarrow \psi_{FSO}^{curr} \leftarrow \mathrm{U}(-\frac{\pi}{2}, \frac{\pi}{2})$ // Azimuth
5 $\quad p.\phi_{FSO} \leftarrow \phi_{FSO}^{curr} \leftarrow \mathrm{U}(-\pi, \pi)$ // Roll
6 $\quad \{\mathcal{P}\} \oplus p$
/* Iterate over generations */
7 **for** $g = 0$ *to* $\mathcal{G}$ **do**
/* Compute eff. contact time (fitness) */
8 $\quad$ **for** p *in* $\{\mathcal{P}\}$ **do**
9 $\quad\quad p.\tau_{\text{eff}} \leftarrow \mathrm{Et}(p.\theta_{FSO}^{curr}, p.\psi_{FSO}^{curr}, p.\phi_{FSO}^{curr})$
/* Tournament selection and crossover */
10 $\quad \{\Lambda\} \leftarrow \{\}$ // Parents
11 $\quad$ **for** i *in* $1, 2, ..., \mathcal{P}$ **do**
12 $\quad\quad T \leftarrow \mathrm{Rs}(S, \{\mathcal{P}\})$ // Random sample
13 $\quad\quad \Lambda \oplus \arg\max_{p \in T} p.\tau_{\text{eff}}$
14 $\quad \{\mathcal{O}\} \leftarrow \{\}$ // Offspring
15 $\quad$ **for** (p_1, p_2) *in* $\{\Lambda\}$ *step* 2 **do**
16 $\quad\quad cp \leftarrow \mathrm{Ri}(1, 3)$ // Random crossover point
17 $\quad\quad \{\mathcal{O}\} \oplus p_1^{\theta,\psi,\phi}[1 : cp] + p_2^{\theta,\psi,\phi}[cp :]$
18 $\quad\quad \{\mathcal{O}\} \oplus p_2^{\theta,\psi,\phi}[1 : cp] + p_1^{\theta,\psi,\phi}[cp :]$
19 $\quad \mathrm{sorted}(\{\mathcal{P}\})[e:] \leftarrow \{\mathcal{O}\}$ // Elites stay
/* Mutation */
20 $\quad$ **for** p *in* $\{\mathcal{P}\}$ **do**
21 $\quad\quad$ **for** α *in* $\{p.\theta_{FSO}, p.\psi_{FSO}, p.\phi_{FSO}\}$ **do**
22 $\quad\quad\quad$ **if** $\mathrm{U}(0, 1) < \Delta_r$ **then**
23 $\quad\quad\quad\quad \alpha \leftarrow \alpha + \mathrm{U}(-\Delta_d, \Delta_d)$
24 $\quad\quad\quad\quad \alpha \leftarrow \max(\min(\alpha, 2\pi), -2\pi)$

Table III: Scenario Parameters

Parameter	Value
Start time t_{start}	01 Jul 2022 00:00 (UTCG)
End time t_{end}	03 Jul 2022 00:00 (UTCG)
Time step t_s	10 s
Propagator	2B
LEO Parameters	
Inclination α_{LEO}	90°, 60°, 30°
LAN Ω_{LEO}	45°
Altitude h_{LEO}	600 km
GEO Parameters	
Inclination α_{GEO}	0°
LAN Ω_{GEO}	0°
Altitude h_{GEO}	35788.12 km
FSO Parameters	
Gimbal elevation $\theta_{gmb}^{\min}$,$\theta_{gmb}^{\max}$	-25°, 180° [17]
Gimbal azimuth $\psi_{gmb}^{\min}$,$\psi_{gmb}^{\max}$	-90°, 90° [17]
Optical Channel Acquisition τ_{acq}	100 s [58]

e) Termination: The algorithm concludes its process by presenting the most optimal individual $p \in \{\mathcal{P}\}$, denoted by the maximum $p.\tau_{\text{eff}}$ value. A unique aspect of GA is that it contains a variety of potentially good placement solutions within the population $\{\mathcal{P}\}$.

V. Evaluation

This section evaluates both the GA and SA methods in a set of realistic satellite scenarios.

Primarily, we analyze a link that extends from a LEO satellite to a GEO relay satellite using a FSO link that emulates the EDRS mission [25], [35], [58] discussed in Section II. Table III outlines the parameters used for these scenarios and the specific orbital characteristics. It's worth mentioning that different LEO inclination angles (α_{LEO}) are evaluated: 90° (polar orbit), 60° (inclined orbit), and 30° (highly inclined orbit). Furthermore, both LEO and GEO nodes maintain orbit eccentricity (e), argument of perigee (ω), and true anomaly (ν) at zero.

The Systems Tool Kit (STK) from Ansys [60] was used to propagate the orbits and export the sequence of target vector $\mathcal{S} = (\{\psi_{tgt}^{SC}\}, \{\theta_{tgt}^{SC}\})$ from the LEO to the GEO satellite from t_{start} to t_{end}. We used the two-body (2B) propagator as it represents satellites with station-keeping capabilities (e.g., thrusters, attitude control) to overcome orbital perturbations. This choice is realistic for satellites equipped with gimbal-based optical inter-satellite links (OISL), such as the EDRS mission. In addition, FSO gimbal elevation and azimuth range were taken from sample FSO data sheets [17]. Finally, we use the parameters listed in Table II regarding the algorithms. It's important to note that the GA will perform $\mathcal{G} \cdot \mathcal{P}_s = 122$ effective contact time evaluations (as represented by the function Et). Conversely, SA will perform $\mathcal{I}_{\max} = 100$ such evaluations. Therefore, both GA and SA demand a similar computational effort.

A. Case Study

To better understand the problem at hand, Fig. 5 showcases timeline plots of two case study solutions for the FSO placement issue in the LEO orbit with 90° inclination. Specifically,

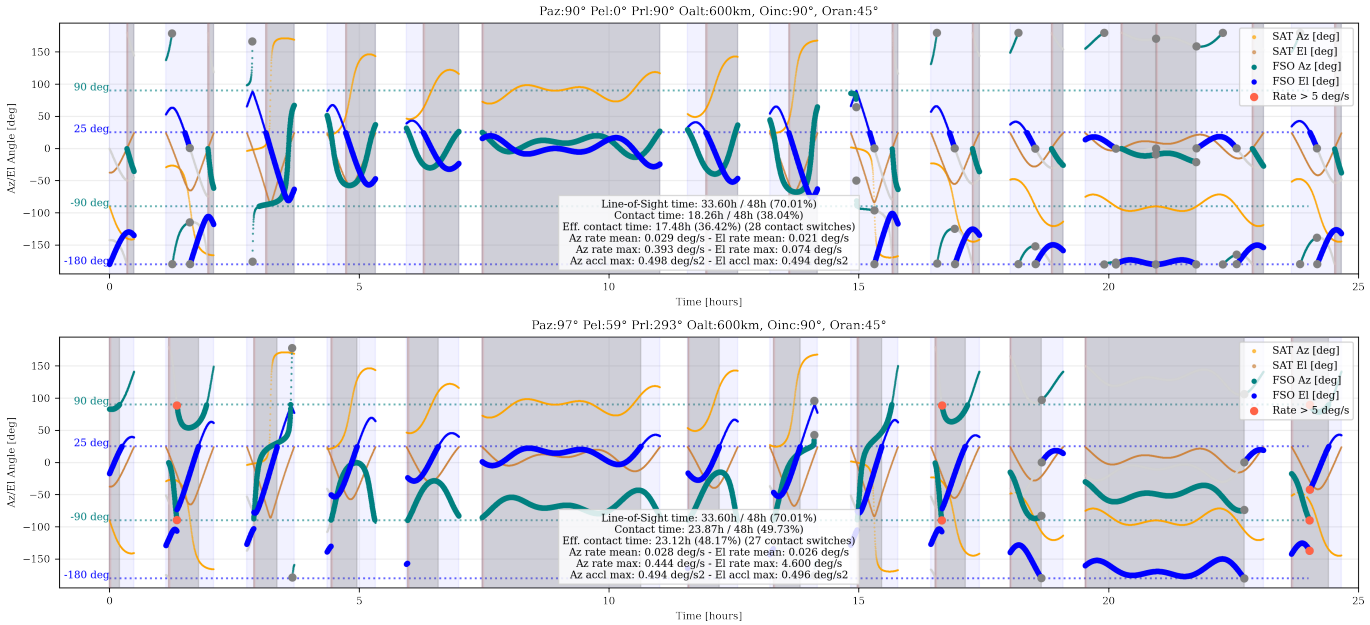

Figure 5: Timeline plots for best baseline (top) and best SA solutions (bottom) for the 90° inclination orbit. These plots compare the baseline solution, representing the default FSO terminal placement, with the optimized placement achieved through SA. The effective contact time and other performance metrics are shown for both configurations.

Fig. 5 a) corresponds to a baseline placement situated on the left face with the top direction. This is equivalent to (θ_{FSO}, ψ_{FSO}, ϕ_{FSO}) = (0, $\frac{\pi}{2}$, $\frac{\pi}{2}$) or $\mathbf{q} = 0.5 + 0.5\mathbf{i} + 0.5\mathbf{j} - 0.5\mathbf{k}$ (refer to Fig. 2 for more details). Conversely, Fig. 5 b) displays the optimal placement derived from the SA method depicted in Algorithm 2. This placement is (θ_{FSO}, ψ_{FSO}, ϕ_{FSO}) = (97°, 59°, 293°).

The timeline plots depict the evolution of the FSO terminal's gimbal angles, with azimuth ψ_{tgt}^{FSO} shown in green and elevation θ_{tgt}^{FSO} in blue. The bold lines indicate the moments when the angle satisfies the visibility constraint, as per lines 7-8 in Algorithm 1. A link with the target satellite is feasible only when both azimuth and elevation fall within the gimbal's permissible range. Horizontal lines are illustrated to designate the gimbal azimuth (-90°, 90°) and elevation (-25°, 180°) limits. Dark gray areas represent periods when a link is feasible, while light grey patches indicate instances where the target satellite is within sight. Still, a link is not feasible due to gimbal constraints. In red, markers are presented to indicate gimbal speed beyond 5 deg/s, which occurs only when gimbals switch between dual positions (see Section III-D *d)*). The plots also provide a view of the azimuth and elevation to the target as observed from the spacecraft frame (ψ_{tgt}^{SC}, θ_{tgt}^{SC}). Furthermore, pertinent numerical data is displayed in text format at the bottom of the plots for reference.

The insights drawn from the timeline plots in Fig. 5 affirm that the SA algorithm was able to ensure effective connectivity 48.17% of the time (out of the 70.01% line-of-sight time), a significant improvement over the baseline's 36.42%. By analyzing the gray regions, it is evident that the SA solution optimally aligns the FSO terminal, maximizing effective visibility duration, especially a the end of the plotted period (t=20 hours). In addition, this solution successfully establishes contacts at the start of the topology period, which were limited when using the baseline placement. In the case of the baseline solution, there are 28 reported instances of contact switches, whereas, for the SA solution, there are 27. This implies that the baseline case suffers from two additional channel acquisition penalties, τ_{acq}, which directly impact the effective contact time, τ_{eff}.

B. General Assessment

In this subsection, we evaluate the general performance of SA and GA as they navigate the solution space. Each potential solution is represented by the plots discussed above.

a) LEO-to-GEO Evaluation: Figures 6 and 7 depict the evolution of the solutions found by SA and GA over iterations (for SA, temperature; for GA, generations) for the LEO-to-GEO scenario studying three different LEO orbits inclinations. The mean effective contact time, denoted as τ_{eff}, is plotted in blue. The shaded blue regions represent the spread of τ_{eff}, i.e., the range between minimum and maximum values. Thin dark green lines within these regions represent the algorithm's multiple search paths throughout the execution. Horizontal grey dotted lines indicate baseline placements.

Table IV presents the numerical outcomes for the obtained τ_{eff} under all evaluated scenarios, including minimum, maximum, and mean effective contact time values throughout all SA and GA executions. Interestingly, results reveal that despite the slight augmentation in computational effort required by GA (122 `Et` evaluations instead of 100), SA outperforms it across all cases. Specifically, SA manages to augment the effective contact time from an average baseline of 35.15% to 45.94% and 47.09% in the average and best case, respectively. This corresponds to an overall improvement of

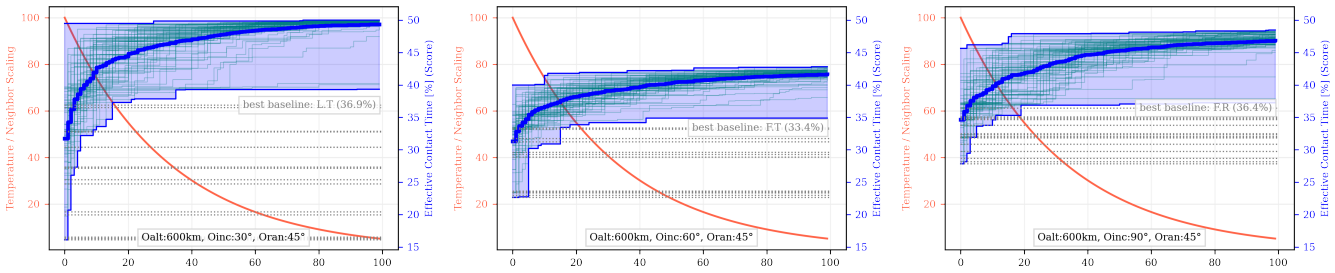

Figure 6: SA evolution for the three reference orbits: 30° (left), 60° (center), and 90° (right) inclination.

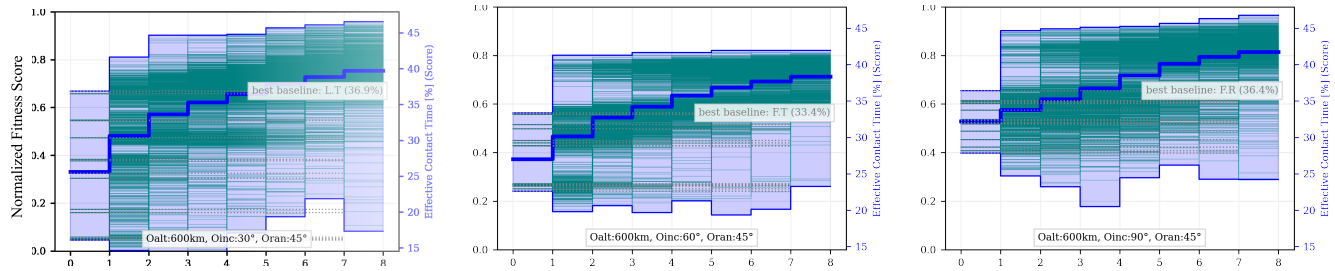

Figure 7: GA evolution for the three reference orbits: 30° (left), 60° (center), and 90° (right) inclination.

Table IV: Effective Contact Time Statistics for SA and GA

	α	$\tau_{\text{eff}}^{\text{baseline}}$	$\tau_{\text{eff}}^{\text{min}}$	$\tau_{\text{eff}}^{\text{mean}}$	$\tau_{\text{eff}}^{\text{max}}$	$\Delta\tau_{\text{eff}}$
SA	90	36.42%	37.23 %	46.83 %	48.45 %	12.03 %
SA	60	33.37%	34.90 %	41.65 %	42.81 %	9.44 %
SA	30	36.87%	39.31 %	49.35 %	50.00 %	13.13 %
Avg	-	35.55 %	37.15 %	45.94 %	47.09 %	11.53 %
GA	90	36.42%	24.22 %	41.75 %	46.78 %	10.36 %
GA	60	33.37%	23.25 %	38.34 %	41.94 %	8.57 %
GA	30	36.87%	17.31 %	39.72 %	46.57 %	9.70 %
Avg	-	35.55 %	21.59 %	39.94 %	45.10 %	9.54 %

Table V: Comparison of Best Baseline (BB), GA, and SA Results: Azimuth (ψ_{FSO}^{max}), Elevation (θ_{FSO}^{max}), and Roll (ϕ_{FSO}^{max}).

α	**Method**	$\tau_{\text{eff}}^{\text{max}}$	ψ_{FSO}^{max}	θ_{FSO}^{max}	ϕ_{FSO}^{max}
30°	BB	17.70 %	0.0°	90.0°	90.0°
	GA	46.57 %	-115°	29°	-5°
	SA	50.00 %	35.02°	35.68°	341.71°
60°	BB	16.02 %	0.0°	90.0°	0.0°
	GA	41.94 %	147°	3°	1°
	SA	42.81 %	128.77°	0.96°	359.63°
90°	BB	17.48 %	90.0°	0.0°	90.0°
	GA	46.78 %	161°	3°	10°
	SA	48.46 %	96.68°	59.17°	293.36°

up to 27.7%. Conversely, in the case of GA, the overall improvement is slightly lower, peaking at 26.8%. However, GA delivers solutions (i.e., individuals) instead of just one, unlocking the potential of future multi-objective extensions. These findings thus underscore the comparative efficacy of SA in finding optimum solutions for the FSO terminal placement. The exact numerical values of the best solutions found in terms of azimuth (ψ_{FSO}^{max}), elevation (θ_{FSO}^{max}), and roll (ϕ_{FSO}^{max}) are provided in Table V. Note that only the best baseline out of the 16 is presented in the table.

b) LEO-to-LEO Evaluation: To validate the performance of the SA and GA methods under different conditions, we carried out a second evaluation campaign involving an LEO-to-LEO inter-satellite link. We considered different inclinations as indicated in Table III. The results validated our earlier findings, demonstrating similar levels of improvement. For SA, the increase in effective contact time was 26.3%, while for GA, it was slightly lower at 25.3%. This reinforces the slight edge that SA has over GA in space-to-space links. Moreover, we found that the more dynamic nature of the LEO-to-LEO scenario posed a challenge to both SA and GA, resulting in a slight reduction in both performances by approximately 1%. The slight reduction in performance observed in LEO-to-LEO links can be attributed to the increased relative motion and frequent changes in pointing requirements. These scenarios impose additional challenges, such as gimbal lock situations and higher link acquisition overheads.

c) Metric Stability Evaluation: Our final evaluation concerns the stability of the τ_{eff} metric beyond the initial 48-hour time horizon for the evaluated scenarios. To this end, we took the best FSO placements from the results in Table IV and examined the τ_{eff} for periods extending up to 30 days. Over this period, the τ_{eff} metric displayed a maximum decrease of 5.6% from the initial value (for instance, a $\tau_{\text{eff}}^{\text{max}}$=48.45% could drop to 46.8% after a month of orbital propagation in the worst case), indicating a relatively stable performance of the system. The mean penalty on τ_{eff} over this period was 2%. The stability of the τ_{eff} metric over extended periods demonstrates the robustness of our optimization methods, ensuring reliable long-term performance despite inherent computational trade-offs. These trade-offs are practical for the intended application, providing a balance between accuracy and efficiency.

Additionally, our proposed SA and GA methods have been designed to accommodate extended time horizons $\mathcal{T}$ in the analysis. In particular, the `Et` function method outlined in Algorithm 1 is prepared for this purpose. However, extending the time horizon would invariably result in increased compu-

tational demands. This inherent trade-off between computational complexity and system performance underscores a key advantage of our SA and GA solutions. As computational capabilities continue to improve, progressively more extensive computation campaigns can be undertaken to optimize real-world FSO placement during spacecraft design.

C. Final Considerations

a) Computational Effort: The computational demands of heuristic-based optimization methods, such as SA and GA, can increase significantly for extended time horizons and high-precision propagators. Modern satellite design and operation rely on high-performance computing (HPC) systems and cloud-based platforms, which provide the necessary computational power. However, potential constraints must be considered: On the one hand, the feasibility of implementing SA and GA for extended time horizons depends on the available computational power. Optimizing the performance of these heuristics through parallelization and efficient use of resources can mitigate some constraints. On the other hand, extended optimization runs can be time-consuming and costly, especially with high-precision numerical propagators.

b) Practical Placement Limitations: It is also relevant to note that practical design constraints may limit the possible positions for placing the FSO terminal on the spacecraft. These constraints could be due to structural, thermal, or other engineering considerations, which might preclude arbitrary placements within the satellite body. Addressing these constraints is crucial for ensuring the feasibility of the proposed optimization in real-world applications. Heuristic methods like GA and SA can be adapted to account for practical constraints by restricting the search space for optimization. This can be achieved by incorporating constraint handling mechanisms into the heuristic algorithms, allowing for the exclusion of specific position ranges that are not feasible for practical design reasons. While our current study does not explicitly address these constraints, we propose this as a direction for future work. By extending the current heuristic methods to include constraint handling, we can ensure that the optimized placements are optimal regarding contact time and feasible from a practical design perspective.

c) Hyperparameter Tuning: Our study found that SA provided better performance regarding improved average contact time than GA. However, it is important to note that this performance difference depends on each method's configuration and choice of hyperparameters. Both SA and GA involve various parameters that significantly influence their optimization performance, and the results presented in our study are associated with the specific hyperparameter settings used. The better performance observed for SA in our study could be linked to a more effective choice of hyperparameters for the given problem. It is important to recognize that different configurations could yield different results, and carefully tuning these parameters is essential for achieving optimal performance with either method.

VI. Conclusion

Our study presents significant advances in optimizing FSO terminal placement using heuristic-based approaches, achieving up to a 27.7% improvement in effective contact time compared to baseline placements. This enhancement translates directly to increased data transfer rates and more reliable communication links, which are crucial for various applications, including Earth observation, disaster management, and real-time global communication.

The proposed SA and GA methods are adaptable to different orbital propagator models, ensuring their applicability across a wide range of satellite missions. The robustness and stability of the τ_{eff} metric over extended periods demonstrate the practical utility of our methods, providing a balance between accuracy and efficiency suitable for real-world operations.

Moreover, the scalability and flexibility of our optimization framework allow for its application to larger satellite constellations and more complex network topologies. The practical implications of these optimizations extend to improving satellite-based internet services, enhancing data collection and transmission in Earth observation missions, and strengthening communication networks in disaster management scenarios.

Future Work: Multiple future research direction emerges from this work. Firstly, performing deeper sensitivity analysis of SA and GA parameters, exploring other multi-objective optimization strategies, and considering multiple FSO terminals, practical placement limitations, and other metrics. This involves not only optimizing for effective contact time but also incorporating additional objectives such as minimizing energy consumption, reducing link acquisition times, and maximizing overall network throughput. Secondly, a further area of interest is the support for space-to-ground links and body-pointing, with some degree of pointing error, which is used for nano-satellite FSO terminals [17]. Lastly, a significant research direction involves effectively studying scheduling azimuth and elevation angles to avoid gimbal lock and considering other propagator models including hybrid propagators.

Acknowledgement

This project has received funding from the European Union's Horizon 2020 research and innovation program under the Marie Skłodowska-Curie grant agreement No 101008233 (MISSION) and the French National Research Agency (ANR) under the project ANR-22-CE25-0014-01.

References

[1] P. K. Sahoo and A. K. Yadav, "A comprehensive road map of modern communication through free-space optics," *Journal of optical communications*, 2020.

[2] K. Samdanis and T. Taleb, "The road beyond 5g: A vision and insight of the key technologies," *IEEE Network*, vol. 34, no. 2, pp. 135–141, 2020.

[3] M. M. Azari *et al.*, "Evolution of non-terrestrial networks from 5g to 6g: A survey," *IEEE communications surveys & tutorials*, 2022.

[4] "Leo small-satellite constellations for 5g and beyond-5g communications," *Ieee Access*, vol. 8, pp. 184 955–184 964, 2020.

[5] J. Du *et al.*, "Cooperative earth observation through complex space information networks," *IEEE wireless communications*, vol. 23, no. 2, pp. 136–144, 2016.

[6] A. Farrag *et al.*, "Satellite swarm survey and new conceptual design for earth observation applications," *The Egyptian journal of remote sensing and space science*, vol. 24, no. 1, pp. 47–54, 2021.

[7] X. Wang *et al.*, "Agile earth observation satellite scheduling over 20 years: Formulations, methods, and future directions," *IEEE Systems Journal*, vol. 15, no. 3, pp. 3881–3892, 2020.

[8] L. He *et al.*, "Joint observation and transmission scheduling in agile satellite networks," *IEEE Transactions on Mobile Computing*, vol. 21, no. 12, pp. 4381–4396, 2021.

[9] P. Wang, H. Li, B. Chen, and S. Zhang, "Enhancing earth observation throughput using inter-satellite communication," *IEEE Transactions on Wireless Communications*, vol. 21, no. 10, pp. 7990–8006, 2022.

[10] F. Jiang, Q. Zhang, Z. Yang, and P. Yuan, "A space–time graph based multipath routing in disruption-tolerant earth-observing satellite networks," *IEEE TAES*, vol. 55, no. 5, pp. 2592–2603, 2019.

[11] J.-H. Lee, J. Park, M. Bennis, and Y.-C. Ko, "Integrating leo satellites and multi-uav reinforcement learning for hybrid fso/rf non-terrestrial networks," *IEEE Transactions on Vehicular Technology*, 2022.

[12] D. Delahaye *et al.*, "Simulated annealing: From basics to applications," *Handbook of metaheuristics*, pp. 1–35, 2019.

[13] S. Mirjalili and S. Mirjalili, "Genetic algorithm," *Evolutionary Algorithms and Neural Networks: Theory and Applications*, pp. 43–55, 2019.

[14] T.-H. Ho, *Pointing, acquisition, and tracking systems for FSO communication links*. University of Maryland, College Park, 2007.

[15] G. Baister and P. Gatenby, "Pointing, acquisition and tracking for optical space communications," *Electronics & communication engineering journal*, vol. 6, no. 6, pp. 271–280, 1994.

[16] G. Baister, P. Gatenby, B. Laurent, and J. Lewis, "Applications for optical free space links in inter-satellite and intra-satellite comms," 1996.

[17] Satsearch, "Optical communications for small satellites and cubesats: product roundup," Jan 2020, accessed: 2023-06-11. [Online]. Available: https://tinyurl.com/fso-product-roundup

[18] R. J. Alliss and B. Felton, "The mitigation of cloud impacts on free-space optical communications," in *Atmospheric Propagation IX*, vol. 8380. SPIE, 2012, pp. 227–238.

[19] D. Giggenbach, "Optical free space links for satellite-ground communications," *Tutorial held at ASMS/SPSC, Livorno*, 2014.

[20] I. Pigulevski, "Optimizing access to space: ground-to-orbit logistics framework (golf)," *New Space*, vol. 5, no. 2, pp. 99–107, 2017.

[21] D. M. Boroson *et al.*, "Overview and results of the lunar laser communication demonstration," in *Free-Space Laser Communication and Atmospheric Propagation XXVI*, vol. 8971. SPIE, 2014, pp. 213–223.

[22] Y. Tang *et al.*, "The availability of space service for inter-satellite links in navigation constellations," *Sensors*, vol. 16, no. 8, p. 1327, 2016.

[23] S. Gong and all, "Network availability maximization for free-space optical satellite communications," *IEEE Wireless Communications Letters*, vol. 9, no. 3, pp. 411–415, 2019.

[24] B. Kopp *et al.*, "Utilizing existing commercial geostationary earth orbit fixed satellite services for low earth orbit satellite communication relays with earth," *New Space*, vol. 7, no. 1, pp. 19–30, 2019.

[25] F. Heine *et al.*, "The european data relay system, high speed laser based data links," in *2014 7th ASMS/SPSC*. IEEE, 2014, pp. 284–286.

[26] C. Zhang *et al.*, "Recent trends in coherent free-space optical communications," in *Metro and Data Center Optical Networks and Short-Reach Links IV*, vol. 11712. SPIE, 2021, pp. 96–109.

[27] D. Giggenbach and A. Shrestha, "Atmospheric absorption and scattering impact on optical satellite-ground links," *Int. Journal of Satellite Comms. and Networking*, vol. 40, no. 2, pp. 157–176, 2022.

[28] N. Devkota *et al.*, "Atmospheric effects on downlink channel of satellite to ground free space optical communications," in *2022 13th ICTC*. IEEE, 2022, pp. 1335–1340.

[29] B. B. Yousif, E. E. Elsayed, and M. M. Alzalabani, "Atmospheric turbulence mitigation using spatial mode multiplexing and modified pulse position modulation in hybrid rf/fso orbital-angular-momentum multiplexed based on mimo wireless communications system," *Optics Communications*, vol. 436, pp. 197–208, 2019.

[30] B. B. Yousif and E. E. Elsayed, "Performance enhancement of an orbital-angular-momentum-multiplexed free-space optical link under atmospheric turbulence effects using spatial-mode multiplexing and hybrid diversity based on adaptive mimo equalization," *IEEE access*, vol. 7, pp. 84 401–84 412, 2019.

[31] E. E. Elsayed, "Atmospheric turbulence mitigation of mimo-rf/fso dwdm communication systems using advanced diversity multiplexing with hybrid n-sm/omi m-ary spatial pulse-position modulation schemes," *Optics Communications*, vol. 562, p. 130558, 2024.

[32] E. E. Elsayed, M. R. Hayal, I. Nurhidayat, M. A. Shah, A. Elfikky, A. I. Boghdady, D. A. Juraev, and M. Morsy, "Coding techniques for diversity enhancement of dense wavelength division multiplexing mimo-fso fault protection protocols systems over atmospheric turbulence channels," *IET Optoelectronics*, 2024.

[33] H. A. Al-Mohammed and E. Yaacoub, "Free space optics communication for ultra-high-speed train running in evacuated tube," *Applied Sciences*, vol. 12, no. 17, p. 8545, 2022.

[34] M. R. Hayal, E. E. Elsayed, D. Kakati, M. Singh, A. Elfikky, A. I. Boghdady, A. Grover, S. Mehta, S. A. H. Mohsan, and I. Nurhidayat, "Modeling and investigation on the performance enhancement of hovering uav-based fso relay optical wireless communication systems under pointing errors and atmospheric turbulence effects," *Optical and Quantum Electronics*, vol. 55, no. 7, p. 625, 2023.

[35] D. Calzolaio *et al.*, "Edrs-c–the second node of the european data relay system is in orbit," *Acta Astronautica*, vol. 177, pp. 537–544, 2020.

[36] G. Tiwari and R. C. S. Chauhan, "A review on inter-satellite links free space optical communication," *Indian journal of science and technology*, vol. 13, no. 6, pp. 712–724, 2020.

[37] A. U. Chaudhry *et al.*, "Free space optics for next-generation satellite networks," *IEEE Consumer Electronics Magazine*, vol. 10, no. 6, pp. 21–31, 2020.

[38] ——, "Temporary laser inter-satellite links in free-space optical satellite networks," *IEEE Open Journal of the Communications Society*, vol. 3, pp. 1413–1427, 2022.

[39] ——, "Laser intersatellite link range in free-space optical satellite networks: Impact on latency," *IEEE Aerospace and Electronic Systems Magazine*, vol. 38, no. 4, pp. 4–13, 2023.

[40] W. S. Rabinovich *et al.*, "Analysis of free space optical (fso) communications and networking using adaptive waveforms for leo satellites," in *Free-Space Laser Communications XXXII*, vol. 11272, 2020, pp. 76–84.

[41] ——, "Modelling of free space optical (fso) communications and networking with low earth orbit (leo) satellites," in *Free-Space Laser Communications XXXIII*, vol. 11678, 2021, p. 1167815.

[42] J. Liang *et al.*, "Link budget analysis for free-space optical satellite networks," in *2022 IEEE 23rd WoWMoM*. IEEE, 2022, pp. 471–476.

[43] M. Goncalves Teixeira *et al.*, "Review on free-space optical communications for delay and disruption tolerant networks," *Electronics*, vol. 10, no. 13, p. 1607, 2021.

[44] R. Navitskaya *et al.*, "Simulation framework for classical and quantum communications over the free-space optical channel," in *Free-Space Laser Communications XXXV*, vol. 12413. SPIE, 2023, pp. 428–441.

[45] B. Bag, A. Das, I. S. Ansari, A. Prokeš, C. Bose, and A. Chandra, "Performance analysis of hybrid fso systems using fso/rf-fso link adaptation," *IEEE Photonics Journal*, vol. 10, no. 3, pp. 1–17, 2018.

[46] O. B. Yahia, E. Erdogan, G. K. Kurt, I. Altunbas, and H. Yanikomeroglu, "A weather-dependent hybrid rf/fso satellite communication for improved power efficiency," *IEEE Wireless Communications Letters*, vol. 11, no. 3, pp. 573–577, 2021.

[47] K. Tekbiyik, G. K. Kurt, A. R. Ektı, and H. Yanikomeroglu, "Reconfigurable intelligent surfaces empowered thz communication in leo satellite networks," *IEEE Access*, vol. 10, pp. 121 957–121 969, 2022.

[48] Y. Xing and T. S. Rappaport, "Terahertz wireless communications: Co-sharing for terrestrial and satellite systems above 100 ghz," *IEEE communications letters*, vol. 25, no. 10, pp. 3156–3160, 2021.

[49] M. Milaševičius and L. Mačiulis, "A review of mechanical fine-pointing actuators for free-space optical communication," *Aerospace*, vol. 11, no. 1, p. 5, 2023.

[50] Defense Mapping Agency, "Department of defense world geodetic system 1984," DMA, TR 8350.2, 1991. [Online]. Available: https://apps.dtic.mil/sti/pdfs/ADA280358.pdf

[51] J. Wertz, D. Everett, and J. Puschell, *Space Mission Engineering: The New SMAD*, ser. Space technology library. Microcosm Press, 2011.

[52] D. A. Vallado, *Fundamentals of astrodynamics and applications*. Springer Science & Business Media, 2001, vol. 12.

[53] N. Salleh *et al.*, "Enhancing simplified general perturbations-4 model for orbit propagation using deep learning: A review," in *Proc. of the 2019 8th ICSCA*, NY, USA, 2019, p. 27–32.

[54] W. Dong *et al.*, "An accuracy analysis of the sgp4/sdp4 model," *Chinese Astronomy and Astrophysics*, vol. 34, no. 1, pp. 69–76, 2010.

[55] A. R. Yaakub and D. J. Evans, "A fourth order runge–kutta rk(4,4) method with error control," *Int. Journal of Computer Mathematics*, vol. 71, no. 3, pp. 383–411, 1999.

[56] J. M. Aristoff *et al.*, "Orbit and uncertainty propagation: a comparison of gauss–legendre-, dormand–prince-, and chebyshev–picard-based approaches," *Celestial Mechanics and Dynamical Astronomy*, vol. 118, pp. 13–28, 2014.

[57] M. Jie and X. Qinbei, "Four-axis gimbal system application based on gimbal self-adaptation adjustment," in *2015 34th Chinese Control Conference (CCC)*. IEEE, 2015, pp. 8866–8871.
[58] Consultative Committee for Space Data Systems, "Optical high data rate (hdr) communication— 1064 nm experimental specification," CCSDS, Tech. Rep. CCSDS 141.11-O-1, 2019.
[59] C. W. Ahn *et al.*, "Elitism-based compact genetic algorithms," *IEEE Trans. on Evolutionary Computation*, vol. 7, no. 4, pp. 367–385, 2003.
[60] "ANSYS Systems Tool Kit (STK)," 2023. [Online]. Available: https://www.ansys.com/products/missions/ansys-stk